Enhancement of adsorption efficiency by surface modified Avocado seed for xylene removal

Rajeshkumar V.[1,*], Chandrakanthamma L.[2], Senthil Kumar M.[3], and Gokulan R.[4,*]

[1]Department of Civil Engineering, KPR Institute of Engineering and Technology, Arasur 641 407, Coimbatore, India

[2]Department of Civil Engineering, Easwari Engineering College, Ramapuram, Chennai 600 087, Tamil Nadu, India

[3]Department of Environmental Engineering, College of Engineering and Technology, Bule Hora University, Bule Hora, West Guji, Ethiopia.
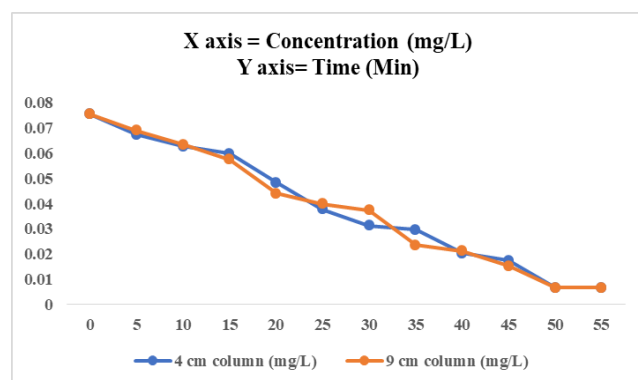
[4]Department of Civil Engineering, GMR Institute of Technology, Rajam 532 127, Andhra Pradesh, India

*to whom all correspondence should be addressed: e-mail: rajeshcit16@gmail.com, gokulan.r@gmrit.edu.in

Graphical abstract

Abstract

The current study work's contribution relates to the removal of xylene using an adsorbent with modified surfaces made from a naturally occurring substance called avocado seed. With the aid of a muffle furnace heated to 600°c, this was converted to become activated carbon. Activated carbon is modified on the surface using titanium di oxide (TiO$_2$). This surface modification demonstrated significant performance in the designated surface area of 67.35 m2 g-1. The varied levels of xylene concentration drop at three distinct temperatures 30, 60, and 90°C were visible. Applying the Thomas and Adams-Bohart to describe equilibrium adsorption data resulted in the model having the highest R^2 values for describing equilibrium isotherm data. SEM patterns captured the degree of the surface modification with increased porosity; however, XRD and FTIR analyses of the surface modified adsorbent did not reveal any structural distortion. This thorough analysis resulted in the efficient removal of 93% of xylene by cost-effective adsorbent.

Key words. Adsorption, surface modification, kinetic study, chromatogram

1. Introduction

The term "xylene" describes the aromatic substances that were regularly present in gasoline. Mostly, it is a synthetic chemical. In small amounts, it is created during forest fires and can also be found naturally in coal tar and petroleum (Marsalek and Svidrnoch, 2020). It smells delicious and is an odourless, combustible liquid. It may also seep into the environment during storage or burial at a waste site, or it may spill accidentally and end up in significant quantities of soil, water, or air (Liu *et al.*, 2020). Because gasoline is kept in subterranean tanks, improper installation, operation, or maintenance could lead to undetected soil and groundwater pollution with a high risk of the undiscovered dissolved contaminant dispersing (Liu *et al.*, 2020). It may descend through the soil and enter underground water below the soil's surface. It takes several months for microscopic organisms to eventually break it down in groundwater (Cao *et al.*, 2020). A worldwide norm for xylene in the range of 0.1- 0.5 mg L-1 was proposed by Public Health England (PHE) (Bisiriyu and Meijboom, 2020). When you breathe xylene vapours, it is most likely to enter your body and contaminate drinking water wells if a significant amount of xylene reaches the soil (You *et al.*, 2020). If you consume or consume water or food that has been tainted with xylene, it also enters your body (Zhao *et al.*, 2016). Acute inhalation exposure to a mixture of toluene and xylenes caused respiratory and neurological toxicity in both people and animals that was more harmful than additive (Zhao *et al.*, 2016). The main effects of prolonged exposure to mixed xylenes in humans, as demonstrated in industrial settings, are neurological (Sharkawy *et al.*, 2016). The most effective approach for separating xylene into individual components and minimal adsorption is called as the adsorption method (Sharkawy *et al.*, 2016). In some ways, this technology offers high productivity and flawless recovery (Yu *et al.*, 2016). Notably, activated carbons continue to be the most extensively investigated adsorbents because of their exceptional high sorption capabilities caused by their distinctive pore architectures and vast surface area (Song *et al.*, 2016). Research is being done to find cheaper, more accessible precursors that can

be used to make activated carbon with surface modification instead of commercial activated carbon (Wang *et al*., 2020). The preparation process and precursor selection affect the structural and textural characteristics of activated carbon (Li *et al*., 2020). However, in order to create a better adsorbent for the efficient adsorption of diverse adsorbates, further modification is occasionally necessary (Xue *et al*., 2020). The use of composite materials to increase the adsorption of activated carbon from aqueous solutions has been well documented in the literature (Wang *et al*., 2020). A naturally occurring composite was noted to have a high xylene adsorption capability and cheap production costs (Xu *et al*., 2019). The adsorption network structure was improved by the decreased weight percentage of the synthetic formation in the natural material, which also increased the composite's capacity for adsorption (Janus *et al*., 2019). Several activated carbon composites have been created and used successfully to remove xylene from aqueous phase (Tucker *et al*., 2016). To the authors' knowledge, very few investigations on TiO₂ impregnation on activated carbon for xylene elimination have been done (Liao *et al*., 2016). The main goal of this study is to investigate how avocado seeds that have been carbonized and surface-modified with titanium dioxide (TiO₂) can be used as an economical adsorbent to remove xylene from aqueous solutions by varying various parameters like pH, contact time, adsorbent dosages, and temperature (Zhou *et al*., 2016). With the use of different isotherms, including the Thomas and Adams-Bohart models, equilibrium data was further examined (Wang *et al*., 2016). To investigate the physical and chemical properties of adsorbents, scanning electron microscopy (SEM), X-ray diffraction, and Fourier transform infrared spectroscopy (FT-IR) were employed (Liao *et al*., 2016).

2. Materials and methods

2.1. Preparation of Column material

The avocado seed was manually broken into several pieces after being gathered and completely dried for 24 hours in a hot air oven at 100°C (Goworek *et al*., 2019). Granular activated carbon was made by completely grinding it (AC) (Liu *et al*., 2019). The carbon material was washed with sodium chloride solution three times to remove the microbiological particles (Yu *et al*., 2019). The carbon material was heated to activate it after being manufactured as adsorbent material at a temperature of 600°C. The sodium perchlorate used in this study was made by oxidizing ammonium chloride to xylene, doubly decomposing it with sodium chloride solution at 100°C, and then cooling the reaction mixture to 100°C to yield sodium perchlorate (Yuvanet *et al*., 2019). Deionized water is used to prepare analytical standards for xylene solutions.

2.2. Modification of the adsorbent

In this study, raw AC material was manufactured and utilized. TiO₂ was the primary contributor to the surface modifications (Gui *et al*., 2019). The AC was sieved and pulverized using a grinder to get the desired grain size (b125 m). The AC sample's chemical makeup was identified (Bi *et al*., 2016). Three-mercaptopropyl trimethoxysilane (MPTMS) (Sigma-Aldrich, Germany) was utilized as a mercapto agent to change the surface of the AC, while TiO₂ (Merck, Germany) served as the solvent (Wu *et al*., 2016). This was the procedure: In the presence of 30 mL TiO₂ solvent, 15 g AC and 15 mL 3-mercaptopropyl trimethoxysilane were activated in a reflux for 6 hours at 60 °C. After filtering with Whatman, No. 42 filter paper, the resultant solid was washed with TiO₂ to remove organ silane chemicals from the AC surface, and it was then dried in an oven at 100 °C (Benjwal *et al*., 2016). After that, it was kept in desiccators for a later use.

2.3. Column study

A glass column with an interior diameter of 3 cm and a length of 90 cm was utilized for the fixed bed column investigations (Sing *et al*., 2016). The AC was used, and the particle sizes started at 0.7mm. AC was used to fill the column, and glass wool was used to cover the bottom (Zhang *et al*., 2019). Beds with heights of 4 and 9 cm were used (Xin *et al*., 2019). The flow rates that were used ranged from 3 to 9 mL/min. After samples were taken at regular intervals, IC calculated the residual xylene content in the effluent samples (Niu *et al*., 2019). Column investigations ended when the column neared fatigue. The column studies are carried out at room temperature for practical purposes.

2.4. HPLC technique

HPLC was used to ascertain the quantity of xylene in the sample using an experimental technique utilizing adsorption. The xylene anion stock standard solutions were obtained, and the water used complied with ISO 4512, Grade 2 (Fang and Guo, 2019). Xylene solution from several sources was used for the technique validation and calibration trials as well as an independent source for quality control (Xiao *et al*., 2019). The HPLC apparatus included a gradient pump with a 20 mL/min flow rate, an auto sampler with an 800 L injection loop, a column C-18 heated to 150°C, an eluent generator supplying 28 mmol/L KOH, and a conductivity detector. Both columns were 3-mm-format PAH CALI suppression columns and Carbon 18 with guard columns. Total running time for each sample was 20 minutes (Decker *et al*., 2017). The operating range, performance, and calibration data for a concentration decade looking at standard solutions of perchlorate concentrations were evaluated statistically.

2.5. Kinetic study

2.5.1. Thomas model

The Thomas model was used to calculate the relationship between solute concentration and time. In continuous column technology, both internal and external mass transfer restrictions were considered (Liu *et al*., 2017).

$$\ln\left(\frac{Co}{Ct}-1\right)=(Kt*q*m/Q)-kt*Co*t$$

where Co and Ct are the influent and effluent concentrations (in mg/L), Kt is the Thomas rate constant (in mL/(min.mg) (Chen *et al*., 2016), and t is the time

(min), A constant flow rate was used to determine the amount of adsorbent in the column, Q (g), and the adsorption kinetics (kt) were determined from the plot of ln [(co/ct)] over time (Ghazy *et al*., 2016). The ranges of regression coefficients serve as a representation of the Thomas model.

2.5.2. Adams-Bohart model

Most often, the Adams Bohart is used to create fixed bed columns. This model was developed under the presumption that external mass transfer resistance and intra-particle diffusion are negligible factors and that the adsorbate is immediately adsorbed onto the adsorbent surface (Ghazy *et al*., 2016). This model is only used to describe the first 10 to 50 percent of the saturation points, or the breakpoint, of the breakthrough curve.

$$\ln\left(\frac{Ct}{Co}\right) = Kab \, Cot - Kab \, Nab\left(\frac{z}{u}\right)$$

In this equation, kab is the kinetic constant (L/mg min), u is the linear flow velocity (cm/min), and Nab is the saturation concentration (mg/L) (Berhane *et al*., 2016). The slope and intercept of the plot of the function ln(Ct/C0) versus t were used to get the parameter values for kab and Nab (Lim and Kim, 2017). The kinetic constant kab changed as the inlet flow rate and initial xylene concentration increased and decreased, respectively (Kohler *et al*., 2017). At higher initial concentrations, Nab's value rose. This may be caused by external diffusion at the beginning of the electro adsorption process (Yan *et al*., 2017). Table 2 displays the R^2, kab, and nab values. The fact that some data did not fit the model perfectly revealed the shortcomings of this model.

2.6. Characterization

With lead K radiation and a scanning speed (3) of 15°/min, the X-ray diffraction (XRD) measurement was made with a Rigaku D/MAX-RB diffractometer (Yahia *et al*., 2017). The applied current and accelerating voltage were 60 kV and 90 mA, respectively. A Nicolet 7200 was used to create

Fourier transform infrared spectra (FT-IR) with Nar as the background (Zhao *et al*., 2017). After 42 scans between 6000 and 600 /cm with a resolution of 5 /cm, the spectra were gathered. Using a scanning electron microscope (SEM, NPLE/MSM-6230LV), the morphologies of the samples were studied. With the help of the vibrating sample magnetometer (VBC, lakeshore/lakeshore 8412) (Blaker *et al*., 2017), the magnetic property of PREC-VBC was examined. A Micromeritics ASAP 4200 adsorption analyzer was used to detect S2 adsorption-desorption isotherms.

2.7. Regeneration of adsorbent

By electrically heating the adsorbent to 470°C in both an inert and an environment with air, thermal regeneration was accomplished (Jayaraju *et al*., 2021). The adsorbent was heated to between 400°C and 600°C in a muffle furnace during the hot water extraction process, twice washed with DI water and a NAOH solution, and then dried for an additional 3 hours in a hot air oven (Dang *et al*., 2017). The ability of the regenerated adsorbent to remove xylene (100 mg/L) was evaluated in order to determine its effectiveness in the regeneration process.

3. Result and Discussion

Continuous process experiments were used to evaluate the adsorption of xylene. For the xylene removal research, samples were gathered every five minutes, and gas chromatography was utilized to determine how well the treatment was working. In the initial phase of the study, AC columns with diameters of 4 cm and 9 cm were baked for two hours at 30°C in a hot air furnace (Zhu *et al*., 2017). While the intake sample level was 3.5 mL/min in 4 cm and 9 cm, the output ranges were 0.6 mL/min and 0.35 mL/min. For both the 4cm and 9cm columns, the treatment's efficacy during the first hour varied between 0.0754mg/L. In 50 minutes, the column was completely exhausted for 4 cm and 9 cm was expressed in Table 1.
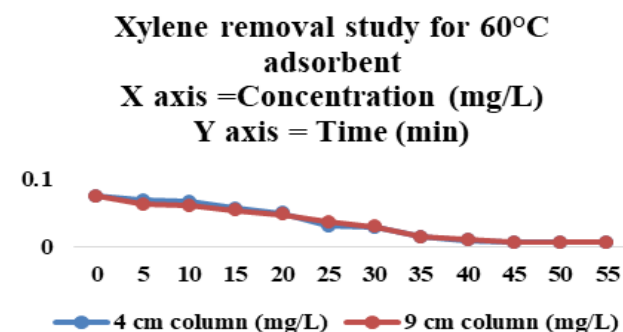
Table 1. Xylene removal study for 30°C adsorbent

Time (min)	4 cm column (mg/L)	9 cm column (mg/L)
0	0.0754	0.0754
5	0.0674	0.0691
10	0.0628	0.0634
15	0.0599	0.0575
20	0.0484	0.0441
25	0.0378	0.0399
30	0.0312	0.0374
35	0.0297	0.0236
40	0.0204	0.0212
45	0.0175	0.0153
50	0.0067	0.0067
55	0.0067	0.0067
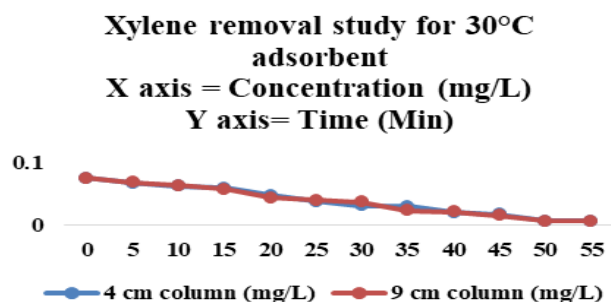
Figure 1. Xylene removal study for 30°C adsorbent

Continuous process experiments were used to study the adsorption of xylene in Table 2. For the xylene removal research, samples were gathered every five minutes, and gas chromatography was utilized to determine how well the treatment was working. In the initial phase of the study, AC columns with diameters of 4 cm and 9 cm were baked for two hours at 60°C in a hot air furnace. While the intake sample level was 3.5 mL/min in 4 cm and 9 cm, the output ranges were 0.6 mL/min and 0.35 mL/min. For both the 4cm and 9cm columns, the treatment's efficacy during the first hour varied between 0.0754mg/L (Lu *et al.*, 2017). In 45 minutes, both different-sized columns ran out of space (Figures 1–4).

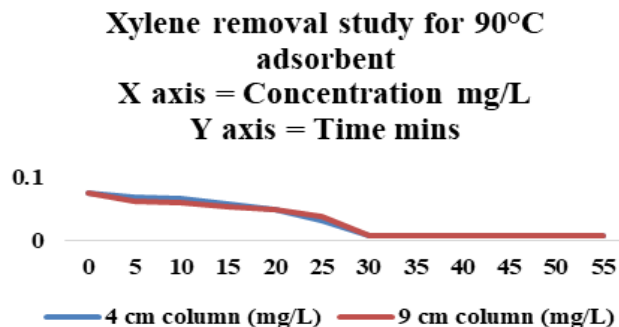**Figure 2.** Xylene removal study for 60°C adsorbent

Figure 3. Xylene removal study for 90°C adsorbent

Continuous process experiments were used to evaluate the adsorption of xylene. For the xylene removal research, samples were gathered every five minutes, and gas chromatography was utilized to determine how well the treatment was working. In the initial phase of the study, AC columns with diameters of 4 cm and 9 cm were baked for two hours at 90°C in a hot air furnace. While the intake sample level was 3.5 mL/min in 4 cm and 9 cm, the output ranges were 0.6 mL/min and 0.35 mL/min. For both the 4cm and 9cm columns, the treatment's efficacy during the first hour varied between 0.0754mg/L. In 30 minutes, both different-sized columns ran out of space.

3.1. Determination of perchlorate by HPLC Technique

The samples were taken after the adsorption research and put in vials that were maintained in the fridge in order to analyse the chromatogram. The intake region received a 20μl sample, which then travelled through the mobile phase and stationary phase. when the ideal perchlorate level was calculated using the gas chromatography output graph. Software was used to analyse the graphical representation, and gas chromatography was employed to ascertain the perchlorate level (zhang *et al.*, 2017). The amount of xylene in the sample was determined based on the height and size of the peak seen in the graphical representation.

Table 2. Xylene removal study for 60°C adsorbent

Time (min)	4 cm column (mg/L)	9 cm column (mg/L)
0	0.0754	0.0754
5	0.0691	0.0633
10	0.0671	0.0612
15	0.0576	0.0545
20	0.0499	0.0484
25	0.0314	0.0371
30	0.0293	0.0299
35	0.0148	0.0152
40	0.0097	0.0103
45	0.0067	0.0067
50	0.0067	0.0067
55	0.0067	0.0067

3.2. Kinetic study
3.2.1. Thomas Model
The adsorption process was regulated by the ionic speciation of the adsorbate that was present in the binding site. The Thomas model was employed in the

evaluation. The consistency of the expected break through curve and the experimental adsorption process were both met. The regression coefficient for 0.0754 mg/L (R^2) for the temperature range of 30°C, 60°C, and 90°C was 0.931. The value of kt depends on the mass (m) and

time of concentration (t). The adsorption kinetics were favourable at the maximum concentration of adsorbate, as evidenced by the lowest kt value at the highest Co. Initial kt values were lower, and at the next level, they increased to 0.017, 0.031 for 30°C, 0.013, 0.008 for 60°C, and 0.027, 0.015 at 90°C with a concentration of 0.0754 mg/L. With increasing bed depth, the rate constant (kt) went up and down. As shown in Tables 3 and 4, there was

a little increase in the equilibrium uptake capacity (qo), which was 21.00, 0.60 for 30°C, 16.71, 0.010 for 60°C, and 0.81, 18.60 for 90°C. The decrease in qo proved that the relationship between bed height and contact time and adsorption capacity is inverse. Reduced influent concentration and flow rate, whereas adsorption is accelerated by higher bed heights (Wang *et al*., 2017).

Table 3. Xylene removal study for 90°C adsorbent

Time (min)	4 cm column (mg/L)	9 cm column (mg/L)
0	0.0754	0.0754
5	0.0691	0.0633
10	0.0671	0.0612
15	0.0576	0.0545
20	0.0499	0.0484
25	0.0314	0.0371
30	0.0067	0.0067
35	0.0067	0.0067
40	0.0067	0.0067
45	0.0067	0.0067
50	0.0067	0.0067
55	0.0067	0.0067

Table 4. Thomas model for Three different study

Material	Column size (cm)	$k_t \times 10^{-3}$ (mL/(min.mg))	q_o (mg/g)	R^2
Avocado Seed 30°C	4	0.017	21.00	0.931
	9	0.031	0.60	0.944
Avocado Seed 60°C	4	0.013	16.71	0.962
	9	0.008	0.010	0.980
Avocado Seed 90°C	4	0.027	0.81	0.931
	9	0.015	18.60	0.953

Table 5. Adams-Bohart model for Three different study

Material	Column size (cm)	Nab (mg/L)	Kab (ml/mg min)	R2
Avocado Seed 30°C	4	272.00	0.0022	0.668
	9	153.35	0.0016	0.702
Avocado Seed 60°C	4	301.50	0.0027	0.653
	9	205.61	0.0019	0.509
Avocado Seed 90°C	4	283.10	0.0012	0.462
	9	289.03	0.0013	0.493

3.2.2. Adams-Bohart model

This model only describes the initial part of the breakthrough curve, from the breakpoint or 10 to 50% of the saturation points. The starting adsorbent concentration, bed height, and inflow flow rate all changed as the kinetic constant Kab did, correspondingly. Nab's value is higher at higher initial solvent concentrations. At the start of the electro adsorption process, external diffusion can be the reason for this. The values for R^2, Kab, and Nab are shown in Table 5. The model had limitations since not all values fit it (Lenin Sundar *et al*., 2020).

3.3. Characterization

3.3.1. Physicochemical properties of the sample

In Figure 5, the synthesized XRD patterns were displayed side by side. Adsorbent's diffraction pattern lacks a crystalline peak, showing that it has an amorphous structure (Figure 5). Instead, it exhibits the typical TiO_2 peaks at 40.6° (320), 46.5° (422), 54.5° (520), 67.8° (622), and 73.8°. (552). The outcomes imply that TiO_2 was successfully incorporated onto the adsorbent's surface. Additionally, no carbon peak was seen, like the XRD patterns of an adsorbent, demonstrating that xylene's amorphous structure persisted following hydrothermal magnetization. Their tiny hysteresis loops, which are

present in the relative pressure P/P0 range between 0.6 and 0.9, further support this. The results of an experiment comparing their pore structure parameters revealed that the adsorbent's surface layer has a lower surface area (3235 m^2/g) and pore volume (2.44 cm^3/g) than the adsorbent (4581 m^2/g and 2.60 cm^3/g, respectively) (Qiu *et al.*, 2014). Due to the magnetic composite's composition of TiO_2, which has a low surface area, and carbonaceous material, which has a high surface area, the specific surface area of the adsorbent is lowered.
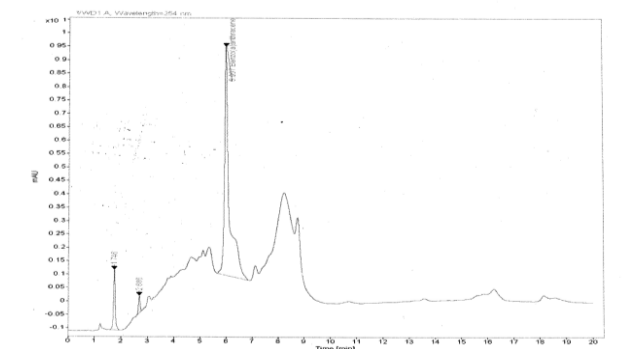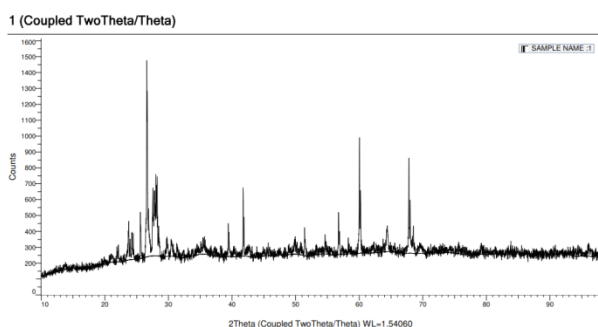

Figure 4. Xylene range obtained by HPLC

Figure 5. XRD pattern of surface modified adsorbent

SEM images were used to analyse the microstructures and morphologies of the adsorbent (Figure 6). The TiO_2 exhibits a honeycomb-like structure with multiple irregular pores, creating more active sites for adsorption (Figure 6). This honeycomb-like structure was well preserved following magnetization, as can be seen in an enlarged SEM image. The TiO_2 spheres have an even coating of decoration and are firmly fixed to the adsorbent's surface. This is consistent with the manufactured magnetic microspheres, which have a diameter of about 200 nm (Lad and Makkawi, 2014). Because TiO_2 altered the surface morphology, uniform dispersion of magnetite on the adsorbent's surface is advantageous for magnetic separation. Figure 6 depicts the various sizes of pores in a block-like construction with a smooth surface.

Figure 7 showed the adsorbent's FTIR spectrum. There are some adsorbed waters and coordinated water present at the same time, as seen by the faint absorption peaks at 4512 and 2678 /cm, which correspond to the stretching vibration and bending vibration of the OH⁻ link, respectively. The peak at 1975 cm for the adsorbent in Figure 7 might be related to the flexural vibration of C-H, while the bands at 1175 cm and 1831 cm are attributable

to the O-H deformation vibration and the C=C stretching vibration, respectively. The large absorption peaks at 1680 cm and 945 cm on the adsorbent are attributed to the carboxyl groups' (-C=O-) and C-H bending vibrations, respectively, as shown in Figure 7. It is due to vibrations of the C-O stretching and O-H bending (in-plane) systems that the broad band between 1574 and 1210 cm was discovered. Using a vibrating sample magnetometer (VSM) at room temperature, the magnetization feature for the modified adsorbent was determined. Figure 7 shows its magnetization curve. displays negligible coercivity and remanence with a saturation magnetization value of 7.15 emu/g, which is smaller than that of the previously reported TiO_2 saturation magnetization (13.376 emu/g and 79.7 emu/g, respectively). The composite's non-magnetic adsorbent is the cause of the observed drop in saturation magnetization (Chen *et al.*, 2014). The spherical TiO_2 particles are firmly fixed on the surface of the adsorbent, as can be observed from the SEM. A magnet placed next to a glass container was used to assess the adsorbent's capacity for magnetic separation. In a short amount of time, the black suspension liquid turns clear, exhibiting outstanding magnetic separation ability.
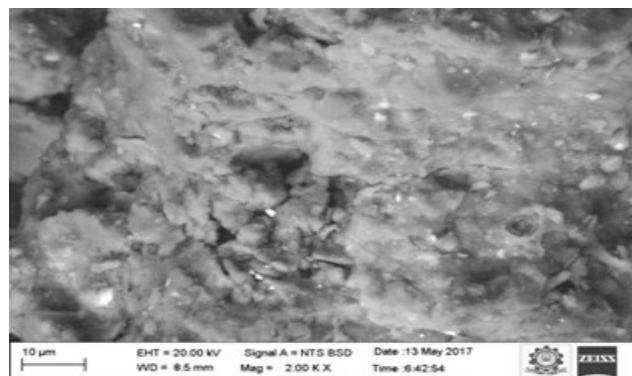

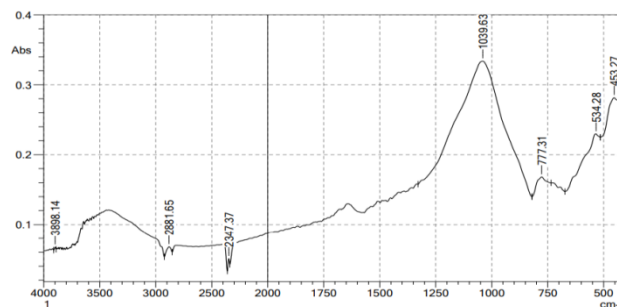**Figure 6.** SEM pattern of surface modified adsorbent

Figure 7. FTIR pattern of surface modified adsorbent

3.4. Regeneration efficiency of adsorbent

The impact of adsorbent recycling times on adsorption capacities Their respective adsorption capabilities are demonstrated to be 0.0754 mg/L after 4 cycles, a decrease of 86.31%, 84.57%, and 81.10% from their original adsorption capacities. The findings demonstrate that the adsorbent has good cyclic adsorption performance with an easy separation characteristic after adsorption as a result of its superior magnetic characteristics, which may more effectively meet the treatment requirements (Wang *et al.*, 2014).

4. Conclusion

As demonstrated by an adsorption study in 4 cm and 9 cm columns in the different temperature (30 °C, 60 °C, and 90 °C) to monitor the influence of temperature in the adsorption study in terms of xylene removal, which proved that the 90 °C is the optimum temperature of the removal efficiency attained in the 90th min for the concentrator, highly functionalized activated carbon derived from avocado seed with surface modification could be further engineered to prepare efficient adsorbents. The TiO_2 before and after adsorption study's viability and morphological changes were demonstrated by the characterization by XRD, SEM, and FTIR. Thomas model and Adam-Boharts model had the best goodness of fit based on correlation coefficient under ideal conditions. According to the findings, surface modified adsorbent has a greater adsorption capacity of nearly 93%. The column efficiency is also rather good in terms of bed capacity up to the breaking point, mass transfer zone, and bed usage. The adsorption capacity of the adsorbent is increased by the addition of TiO_2 to activated carbon, and column regeneration shown that after 4 cycles, the efficiency of the column was around 0.0754 mg/L, a reduction of 86.31%, 84.57%, and 81.10% from their initial adsorption capacities. Which demonstrated the various ways columns were used to remove xylene.

References

Benjwal P., Sharma R., and Kar K.K. (2016). Effects of surface microstructure and chemical state of featherfiber-derived multidoped carbon fibers on the adsorption of organic water pollutants. *Materials and Design*, **110**, 762–774.

Berhane T.M., Levy J., Krekeler M.P.S., Danielson N.D. (2016). Adsorption of bisphenol A and ciprofloxacin by palygorskite-montmorillonite: Effect of granule size, solution chemistry and temperature. *Applied clay science*, **132**, 518–527.

Bi H., Jiang Z., Li J., Li P., Chen L., Pan Q., and Wu Y. (2016). The Ono–Kondo model and an experimental study on supercritical adsorption of shale gas: A case study on Longmaxi shale in southeastern Chongqing, China. *Journal of natural gas science and engineering*, **35**, 114–121.

Bisiriyu I.O., and Meijboom R. (2020). Adsorption of Cu(II) ions from aqueous solution using pyridine-2,6-dicarboxylic acid crosslinked chitosan as a green biopolymer adsorbent. *International Journal of Biological Macromolecules*, 165, 2484–2483.

Blaker C., Christiophpasel., Luckas M., Dreisbach F., Bathen D. (2017). Investigation of load-dependent heat of adsorption of alkanes and alkenes on zeolites and activated carbon. *Microporous and mesoporous materials*, 241, 1–10.

Cao H., Wu X., Shatir S., Zhang A.S.H., and Mood S.H. (2020). Characteristics and mechanisms of phosphorous adsorption by rape straw-derived biochar functionalized with calcium from eggshell. *Bioresource Technology*, **318**, 124063.

Chen J., Cao F., Chen S., Jiang M., Cen N.X.G. (2014). Adsorption kinetics of NO on ordered mesoporous carbon (OMC) and cerium-containing OMC (Ce-OMC). *Applied Surface Science*, **317**, 26–34.

Chen S.J., Fu Y., Huang Y.X., Tao Z.C., and Zhu M. (2016). Experimental investigation of CO_2 separation by adsorption methods in natural gas purification. *Applied Energy*, **179**, 329–337.

Dang S., Zhao L., Yang Q., Zhang M., Zhang J., Gao J., Xu C. (2017). Competitive adsorption mechanism of thiophene with benzene in FAU zeolite: The role of displacement. *Chemical Engineering Journal*, **328**, 172–185.

Decker J.D., Folens K., Clercq J.D., Meledina M., Tendeloo G.V., Laing G.D, and Voort P.V. (2017). Ship-in-a-bottle CMPO in MIL-101(Cr) for selective uranium recovery from aqueous streams through adsorption. *Journal of hazardous materials*, **335**, 1–9.

El-Sharkawy M.M., Askalany A.A., Harby K., and Ahmed M.S. (2016). Adsorption isotherms and kinetics of a mixture of Pentafluoroethane, 1,1,1,2-Tetrafluoroethane and Difluoromethane (HFC-407C) onto granular activated carbon. *Applied thermal Energy*, **93**, 988–994.

Fang Y.G., and Guo L.F. (2019). Experimental study on the influence of water adsorption effect on water fluidity under different electric field strength. *Chemical Physical letters*, **735**, 136768.

Ghazy M., Askalany A.A., Harby K., Ahmed M.S. (2016). Adsorption isotherms and kinetics of HFC-404A onto bituminous based granular activated carbon for storage and cooling applications. *Applied Thermal energy*, **105**, 639–645.

Ghazy M., Harby, Ahamed, Askalany A., Bidyut, Saha B. (2016). Adsorption isotherms and kinetics of activated carbon/Difluoroethane adsorption pair: Theory and experimentsIsothermes et cinétique d'adsorption d'une paire d'adsorption de carbone actif/difluoroéthane: théorie et expériences. *International journal of refrigeration*, **70**, 196–205.

Goworek J., FaniaK W., and Zaleski R. (2019). Study of swollen crosslinked polymers by low-temperature adsorption of nitrogen using blocking siloxane agent. *Polymer Testing*, **79**, 105990.

Gui Y., Chen J., Wang W., Zhu Y., Tang C., and Xu L. (2019). Adsorption mechanism of hydrogen sulfide and sulfur dioxide on Au–MoS2 monolayer. *Superlattices and micro structures*, **135**, 106280.

Janus R., Wadrzyk M., Natkanski P., Cool P., and Kustrowski P. (2019). Dynamic adsorption–desorption of methyl ethyl ketone on MCM-41 and SBA-15 decorated with thermally activated polymers. *Journal of industrial Engineering and chemistry*, **71**, 465–480.

Jayaraju R.M., Gaddam K., Ravindiran G., Palani S., Paulraj M.P., Achuthan A., Saravanan P., Muniasamy S.k. (2021). Biochar from waste biomass as a biocatalyst for biodiesel production: an overview, *Applied Nano science*.

Kohler T., Hinze M., Muller K., Schwieger W. (2017). Temperature independent description of water adsorption on zeotypes showing a type V adsorption isotherm. *Energy*, **135**, 227–236.

Lad J., Makkawi Y T. (2014). Adsorption of dimethyl ether (DME) on zeolite molecular sieves. *Chemical Engineering Journal*, **256**, 335–346.

Li S., Song K., Yu L., Rwiza J., Zhao R.D., and Diao R. (2020). Study on co-adsorption mechanisms of benzene and toluene on activated carbon via molecular simulation. *Materials Letters*, **280**, 128554.

Liao B., Sun W.Y., Guo N., Ding S.L., and Su S.J. (2016). Comparison of CO_2^+ adsorption by chitosan and its triethylene-tetramine derivative: Performance and mechanism. *Carbohydrate Polymers*, **151**, 20–28.

Liao B., Naguo W.Y., Ding S.J., and Su S.J. (2016). Equilibriums and kinetics studies for adsorption of Ni(II) ion on chitosan and its triethylenetetramine derivative. Colloids and surfaces A: *Physicochemical and Engineering aspects*, **501**, 32–41.

Lim Y.S., Kim J.H. (2017). Isotherm, kinetic and thermodynamic studies on the adsorption of 13-dehydroxybaccatin III from Taxus chinensis onto Sylopute. *The journal of chemical thermodynamics*, **115**, 261–268.

Liu D.G., Zhang X., Zhang C., and Yuvan S. (2019). Adsorption of C5Pe molecules on silica surfaces with different hydrophobicity studied by molecular dynamics simulation. *Applied surface science*, **495**, 143624.

Liu W., Ren Q., Wu R., Wang B., Hu, Hou Q., and Ni Y. (2020). Insight on adsorption of cellulase on wet ground corncob residues and its evaluation by multivariate linear analysis. *Bioresource Technology*, 318, 124107.

Liu X., Wu C., Wei G., Zhang X., and Jia T. (2020). Adsorption deformation characteristics of coal and coupling with permeability during gas injection. *Journal of Petroleum Science and Engineering*, 195, 107875.

Liu Y.H., Duan X., Cao X., Che D., and Liu K. (2017). Experimental study on adsorption of potassium vapor in flue gas by coal ash. *Powder Technology*, **318**, 170–176.

Lu F., Huang C., You L., YinY., Zhang Q. (2017). Cross-linked amino konjac glucomannan as an eco-friendly adsorbent for adsorption of Cr(VI) from aqueous solution. *Journal of molecular liquid*, **247**, 141–150.

Marsalek R., and Svidrnoch M. (2020). The adsorption of amitriptyline and nortriptyline on activated carbon, diosmectite and titanium dioxide. *Environmental Challenges*, **01**, 100005.

Niu F., Cai M., Pang J., Xiaoling, Yang D., and Zhang G. (2019). Gas molecular adsorption effects on the electronic and optical properties of monolayer SnP3. *Vacuum*, **168**, 108823.

Qiu X., Li N., Ma X., Yang S., Xu Q., Li H., Lu J. (2014). Facile preparation of acrylic ester-based crosslinked resin and its adsorption of phenol at high concentration. *Journal of Environmental chemical Engineering*, **02**, 745–751.

Saffarionpour S., Sevillano D.M., Wielen L.A.M.V.D., Noordman T.R., Brouwer E., and Ottens M. (2016). Selective adsorption of flavor-active components on hydrophobic resins. *Journal of chromatography A*, **1476**, 25–34.

Sing H., Yang G., Song H.L., Cui X.H., Li F., and Yuan D.D. (2016). Kinetic and thermodynamic studies on adsorption of thiophene and benzothiophene onto AgCeY Zeolite. *Journal of the Taiwan Institute of Chemical Engineers*, 63, 125–132.

Song G., Zhu X., Liao R.C., Dong Y., and Chen D.L. (2016). An investigation of CO2 adsorption kinetics on porous magnesium oxide. *Chemical Engineering Journal*, 283, 175–183.

Sundar M.L., Aravindan A., Sujatha S., Mahendran S., Kalyani G., Zunaithur Rahman D., Vijayakumar A., Senthil Kumar M. (2020). Biochar derived from Caulerpa scalpelliformis for the removal of Reactive Yellow 81 in batch and packed bed column., *Biomass Conversion and Biorefinery*.

Tucker I.M., Petkov J.T., Penfold J., Thomas R.K., Cox A.R., and Hedges N. (2016). Adsorption of hydrophobin/β-casein mixtures at the solid-liquid interface. **Journal of colloid and interface science**, **478**, 81–87.

Wang D., Zhang J., Yang Q., NaLi, Sumathy K. (2014). Study of adsorption characteristics in silica gel–water adsorption refrigeration. *Applied Energy*, 113, 734–741.

Wang H., Qu Z.G., Zhou. (2017). A combined GCMC and LBM simulation method for CH_4 capture in Cu-BTC particle adsorption bed. *International communication in heat and mass transfer*, **88**, 48–53.

Wang H., Shen J., Wu Y., Sun X., Zhou Y., and Ke Y. (2020). A subtraction fitting method for independent determination of enantioselective and nonselective adsorption isotherms based on the single-component isotherms in the framework of the two-site model. *Journal of Chromatography A*, **1632**, 461608.

Wang X., Chen A., Chen B., and Wang L. (2020). Adsorption of phenol and bisphenol A on river sediments: Effects of particle size, humic acid, pH and temperature. *Ecotoxicology and Environmental safety*, **204**, 111093.

Wang Y., Chen Y., Xie H., Zhang C., and Zhan L. (2016). Lead adsorption and transport in loess-amended soil-bentonite cut-off wall. *Engineering Geology*, **215**, 69–80.

Wu S., Tang D., Li S., Chen H., and Wu H. (2016). Coalbed methane adsorption behavior and its energy variation features under supercritical pressure and temperature conditions, *Journal of Petroleum science and Engineering*, **146**, 726–734.

Xiao J., Zhang J., Lv W., Song Y., and Zheng Q. (2019). Multifunctional graphene/poly(vinyl alcohol) aerogels: In situ hydrothermal preparation and applications in broad-spectrum adsorption for dyes and oils. *Carbon,* 123, 354–363.

Xin F., Xu H., Tang D., and Cao L. (2019). Properties of lignite and key factors determining the methane adsorption capacity of lignite: New insights into the effects of interlayer spacing on adsorption capacity. *Fuel Processing Technology*, **196**, 106181.

Xu W., Chen Y.X., Zhamg W.S., and Li B. (2019). Fabrication of graphene oxide/bentonite composites with excellent adsorption performances for toluidine blue removal from aqueous solution. *Advanced powder Technology*, 30, 493–501.

Xue P., Zhang L., Liang Q., Sun X., Zhao Q., and Qi P. (2020). Thermodynamic characteristics of CH4 adsorption by continental shale: A case study of the Upper Triassic Yanchang shale in the Yanchang Gasfield, Ordos Basin. *Natural Gas Industry B*, **07**, 267–277.

Yahia M.B., Salahknani., Hsan L.B.H., Yahia M.B., Nasri H., Lamine A.B.L. (2017). Statistical studies of adsorption isotherms of iron nitrate and iron chloride on a thin layer of porphyrin. *Journal of molecular liquids*, **248**, 235–245.

Yan Y., Sun K., Sun Y., Zhang Y., Guo J., Dengc L., Che D. (2017). Adsorption and Agglomeration Characteristics of Ash Particles after Reducing Flue Gas Temperature below the Acid Dew Point. *Energy Procedia*, **142**, 3301–3306.

You L., Xu K., Ding G., Shi X., Li J., and Wang S. (2020). Facile synthesis of Fe3O4@COF covalent organic frameworks for

the adsorption of bisphenols from aqueous solution. *Journal of Molecular Liquids*, 320, 114456.

Yu F., Sun S., Han S., Zheng J., and Ma J. (2016). Adsorption removal of ciprofloxacin by multi-walled carbon nanotubes with different oxygen contents from aqueous solutions. *Chemical Engineering Journal*, **285**, 588–595.

Yu W., Xu H., Roden E.E., and Wan Q. (2019). Efficient adsorption of iodide from water by chrysotile bundles with wedge-shaped nanopores. *Applied clay science*, **183**, 105331.

Yuvan Y., Dong X., and Sandoval L.R. (2019). A density functional theory analysis on syngas adsorption on NiO (100) surface. *Applied surface science*, **498**, 143782.

Zhang L., Jain G., Puerto M., Southwick E., Hirasaki G., and Biswal S.L. (2019). Static adsorption of a switchable diamine surfactant on natural and synthetic minerals for high-salinity carbonate reservoirs. *Colloids and Surfaces A. Physicochemical and Engineering Aspects*, **583**, 123910.

zhang Y., Yan Y., Liu J., Qi Q., Deng L., Che D. (2017). Adsorption Characteristics of Sulfuric Acid Mist on Fly Ash in Low-low temperature Flue Gas System. *Energy Procedia*, **142**, 3307–3312.

Zhao J., Yao J., Zhang L., Sui H., and Zhang M. (2016). Pore-scale simulation of shale gas production considering the adsorption effect. *International Journal of heat and mass transfer*, **103**, 1098–1107.

Zhao X., Chen B., Han L., Wen C., Yu X., Chang L., Wang J., Feng G., Liu J.A. (2017). Density functional study on H2S adsorption on Pd(111) and Pd/γ-Al2O3(110) surfaces. *Applied surface science*, **423**, 592–601.

Zhao Y.W., Xian B., Hui S., Zhan G.X., and Liu J.C. (2016). Adsorption of dimethyl disulfide on ZSM-5 from methyl tert-butyl ether liquid: A study on equilibrium and kinetics. *Fuel Processing Technology*, **145**, 14–19.

Zhou D., chaofeng Z., Zhao D., Zhao Y.S., and Cai T.T. (2016). Uniformity of temperature variation in coal during methane adsorption. *Jounral of natural gas science and Engineering*, 33, 954–960.

Zhu C., Shi Y., Cai N. (2017). High-pressure carbon dioxide adsorption kinetics of potassium-modified hydrotalcite at elevated temperature, *Fuel*, **207**, 579–590.